

A Self-Ordered Nanostructured Transparent Electrode of High Structural Quality and Corresponding Functional Performance

Dirk Döhler, Andrés Triana, Pascal Büttner, Florian Scheler, Eric S.A. Goerlitzer, Johannes Harrer, Anna Vasileva, Ezzeldin Metwalli, Wolfgang Gruber, Tobias Unruh, Alina Manshina, Nicolas Vogel, Julien Bachmann, and Ignacio Mínguez-Bacho*

The preparation of a highly ordered nanostructured transparent electrode based on a combination of nanosphere lithography and anodization is presented. The size of perfectly ordered pore domains is improved by an order of magnitude with respect to the state of the art. The concomitantly reduced density of defect pores increases the fraction of pores that are in good electrical contact with the underlying transparent conductive substrate. This improvement in structural quality translates directly and linearly into an improved performance of energy conversion devices built from such electrodes in a linear manner.

which (>95%) are electrically contacted to an underlying transparent conducting substrate, has still not been demonstrated. This type of structure is of high interest for the investigation and modeling of charge transport in photovoltaic systems and is demonstrated in this study.

Gaining control over the morphology of thin films is one of the most critical challenges in nanomaterials science and engineering for the development of energy storage and conversion technologies and devices. A common phenomenon occurring

in energy storage and conversion technologies is the transport of charges between nanostructured electrodes. Efficient charge transport should occur in well-defined straight pathways.^[1–5]

A wide variety of methods exist to fabricate nanostructured materials. These methods can be differentiated in bottom-up and top-down approaches. Bottom-up approaches are typically inexpensive, allow for upscaling and their fabrication parameters are flexible, enabling the adjustment of shape and sizes of nanostructures.^[6–12] However, the control over the morphology is limited. Top-down methods provide outstanding control of the nanomaterials geometry and arrangement.^[13–18] Nevertheless, these techniques typically require expensive equipment and are slow fabrication processes.

Aluminum anodization is a bottom-up technique that results in the formation of nanopores arrays in acidic electrolytes.^[19] The geometric parameters of these nanostructures can be adjusted by tuning the type of electrolyte, its acid concentration, voltage and current of the anodization process.^[20–29] Depending on the experimental parameters applied, the anodizations are typically differentiated in mild and hard anodization regimes.^[30–33] The alternation between both regimes during the electrochemical oxidation enables the modification of the geometry of the pores in the course of the anodization.^[34–38] A simple approach to controlling the geometric parameters and to obtaining ordered arrays of nanopores is to use a structure-guiding template. The most extended and widely used method to achieving ordered nanoporous structures is the two-step anodization method. This method forms ordered arrays based on a self-assembly process and it is restricted to some specific experimental conditions combining voltage and electrolytes, requires anodization times of several hours and the use of particularly hazardous chemicals (chromic acid) to dissolve disordered pores selectively.

1. Introduction


Despite the broad variety of chemical and physical methods of nanostructure preparation available, the self-assembled generation of highly ordered, parallel arrays of cylindrical, short (<1 μm), straight nanopores (diameter <500 nm), most of

D. Döhler, A. Triana, P. Büttner, F. Scheler, Prof. J. Bachmann, Dr. I. Mínguez-Bacho
Chemistry of Thin Film Materials, Department of Chemistry and Pharmacy, IZNF
Friedrich-Alexander University of Erlangen-Nürnberg
Cauerstr. 3, 91058 Erlangen, Germany
E-mail: ignacio.minguez@fau.de

E. S. A. Goerlitzer, J. Harrer, Prof. N. Vogel
Institute of Particle Technology
Friedrich-Alexander University Erlangen-Nürnberg
Cauerstraße 4, 91058 Erlangen, Germany

A. Vasileva, Prof. A. Manshina, Prof. J. Bachmann
Institute of Chemistry
Saint-Petersburg State University
Universitetskii pr. 26, St. Petersburg 198504, Russia

Dr. E. Metwalli, Dr. W. Gruber, Prof. T. Unruh
Institute for Crystallography and Structure Physics
Friedrich-Alexander University Erlangen-Nürnberg
Staudtstrasse 3, 91058 Erlangen, Germany

 The ORCID identification number(s) for the author(s) of this article can be found under <https://doi.org/10.1002/smll.202100487>.

© 2021 The Authors. Small published by Wiley-VCH GmbH. This is an open access article under the terms of the Creative Commons Attribution-NonCommercial-NoDerivs License, which permits use and distribution in any medium, provided the original work is properly cited, the use is non-commercial and no modifications or adaptations are made.

DOI: 10.1002/smll.202100487

Top-down techniques present an alternative to the traditional two-step aluminum anodization providing long-range ordered nanopore arrays. A variety of techniques and methodologies have been employed and developed to achieve these highly ordered structures, for example, via laser interference lithography,^[39,40] nanoimprint,^[41–43] flash nanoimprint,^[44] focused ion beam,^[38,45] or holographic lithography.^[46] Nanosphere lithography (NSL) uses self-assembled polymer or silica spheres as a template to form a periodic pattern.^[47,48] In comparison with other lithography techniques, NSL is inexpensive, and does not require very specialized or complex equipment. The sphere sizes can be controlled in a wide range from micrometers to tens of nanometers.^[49] NSL combined with anodic anodization constitute a powerful tool to manufacture periodic anodic aluminum oxide (AAO) nanostructures.^[50–54] NSL has recently been applied to fabricating a unique hierarchical system composed of arrays of nanopores radially distributed within hexagonally arranged unit cells that antireplicate the PS spheres pattern.^[55]

This highly ordered system has been used as a template for a variety of applications in which the pores have been filled or coated with magnetic materials, polymers, organic and inorganic semiconductors.^[35,56–62] However, since the optical properties of AAO are highly tunable,^[63–69] it is of particular interest to the photovoltaic community. Light absorption, charge transport, and in the case of hybrid perovskites the confinement in a matrix that suppresses degradation and ion migration, have all been shown to potentially improve the performance of solar cells.^[70] Furthermore, confinement can influence the crystallization of functional semiconductors.^[71,72]

Some applications benefit from high aspect ratio structures, others require short pathways due to the short diffusion length of charge carriers.^[73,74] In the later case, the use of ultra-short (<500 nm) nanochannels is required. Elaborate and careful procedures have been developed to transfer the AAO layers to other substrates while overcoming the difficulties of working with layers of such a poor mechanical stability.^[75,76] Therefore, the direct growth of nanoporous AAO on transparent and conductive substrates is the logical but challenging solution in the pursuit of opto-electronic applications. The direct anodization of Al on transparent conductive oxides (TCO) is troublesome due to oxygen evolution reaction and subsequent delamination issues during the electrochemical process.^[77] This limitation can be overcome by introducing a valve-metal between the TCO and the Al layer.^[78] However, this approach presents two important limitations. First, the oxidation of the valve-metal generates an amorphous insulating layer that must be dissolved in a subsequent step. Second, the thickness of that insulating layer presents significant inhomogeneities, which render the subsequent etching of undesired oxide at the interface imperfect.^[79] This means that a fraction of pores is left electrically insulated by remnants of oxide at their extremity. Anodization of pre-patterned aluminum substrates would help to mitigate inhomogeneities of the anodic layer, however the remaining barrier layer or the opacity of some of the constituting materials limits the application of this strategy in solar energy conversion.^[53,54,80]

In this work, we present a fabrication method to grow highly ordered arrays of ultrashort alumina nanopores via one-step anodization of aluminum evaporated on transparent electrodes, and

we demonstrate its application in a solar cell. We introduce an anatase TiO₂ layer between the ITO and the Al layer, and we use nanosphere lithography to generate a transparent electric insulator (SiO₂) pattern on the Al surface. The homogeneity of the nanoporous geometry allows for a perfectly uniform dissolution of the insulating barrier layer at the extremity of all the pores. This enables its functionalization as a nanostructured transparent electrode. To demonstrate the functionality of the nanostructured transparent electrodes, we fabricate Sb₂S₃ solar cells based on uniaxial nanostructures with highly controlled geometries that go beyond the conventional mesoporous and planar architectures. This model system presents the potential to adjust individually its geometric parameters (i.e. diameter between 100 and 300 nm, length between 100 nm and 1 μm, light absorber thickness between 1 and 50 nm) to optimize the performance of any solar energy conversion device depending on its opto-electronic properties. For the current study we fix the pore length according to the charge carrier diffusion length and the diameter to two individual values consistent with the self-ordering regime of anodization in two different electrolytes. The high degree of order is crucial to the performance. The reduced density of defect pores translates directly into an increased fraction of p-i-n heterojunctions in proper electrical contact with the underlying transparent conductor. We find a linear relationship between degree of order exhibited by the template and the short-circuit current reached by the device.

2. Results and Discussion

2.1. Preparation of Highly Ordered Nanoporous AAO on Transparent Substrates

Our substrate consists of a commercial transparent conducting oxide (TCO) glass slide, with a 200 nm thick indium tin oxide (ITO) layer as the TCO. ITO is chosen (instead of fluorine-doped tin oxide, FTO) for its smooth surface. A rough surface would cause deleterious inhomogeneities in the subsequently deposited layers. A TiO₂ layer of 50 nm is then deposited via sputter-coating. The as-deposited TiO₂ layer is amorphous and is converted to the anatase phase upon annealing in air for 30 min at 500 °C. The anatase TiO₂ interlayer plays a crucial role in preventing electric breakdown and delamination in the final stages of anodization.^[81] To complete the stack of layers to be anodized, we evaporate an Al layer of 200 nm. SEM micrographs reveal a grainy yet rather compact morphology of the Al layer (**Figure 1a,b**). The surface of the Al is perfectly homogeneous and crack-free over large areas (see **Figure S1**, Supporting Information). The grazing incident X-ray diffraction (GIXRD) pattern confirms the formation of TiO₂ in anatase phase and a high quality Al film with preferential crystal orientation along the [111] axis.

A dispersion of polystyrene (PS) spheres of 280 nm is spread on an air–water interface. The dispersion is carefully prepared adjusting concentration of PS spheres to 4 wt% and by adding ethanol to facilitate spreading on the air/water surface, and a 0.1 M HCl solution in the right ratio to prevent spheres from sinking and improve significantly the self-assembling process. The self-assembled monolayer prepared on the water surface displays a bluish color due to light scattering. It is then transferred

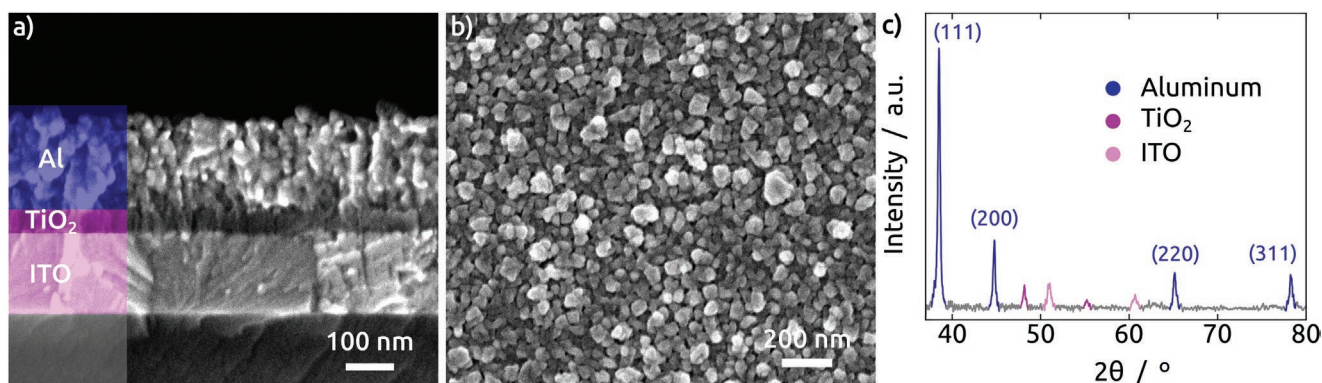


Figure 1. SEM micrograph of a) the cross-section of the stack of layers (from bottom to top: ITO, TiO₂ and Al); b) top-view of the Al layer evaporated on TiO₂; c) X-ray diffraction pattern of the starting stack of layers.

to the ITO/TiO₂/Al substrate without alteration in the quality of the order (Figure 2b). At this stage, we observe very large areas with uniform hexagonal close-packed domains, on the order of several thousand μm² (Figure S2, Supporting Information). Nevertheless, the monolayer is not defect-free, although these defects are only local and do not alter the hexagonal order of the surrounding spheres. The defect density calculated from images in Figure S3, Supporting Information is 3.9%.

From there, the pre-patterning process continues in two steps as described in Figure 2a. First, the samples are exposed to oxygen plasma to reduce the diameter of the PS spheres. This anisotropic plasma etch causes the PS spheres to lose their original shape and flatten to an oval shape (Figure S4, Supporting Information).^[49] Laterally, gaps are generated between them without affecting the hexagonal order. At this point, the system consists of a non-close-packed arrangement of spheres with diameter of 180 nm (Figure 2c). Second, a SiO₂ layer of 40 nm is then generated on the Al/PS spheres substrate surface by reactive evaporation from SiO. After subsequent removal of the PS spheres, the surface features a SiO₂ nanohole array with hexagonally ordered openings that expose the underlying Al.

They reproduce the hexagonal arrangement formed originally by the PS spheres perfectly (Figure 2d). The roughness visible inside the opening in Figure 2d is that of the Al metal layer, demonstrated by the smooth topography obtained on a Si/SiO₂ wafer (Figure S5, Supporting Information). The AFM profile quantifies the SiO₂ film thickness to 40 nm.

The Al/SiO₂ hexagonally ordered pattern is now anodized at 0 °C in a two-electrode setup in three different conditions: a) 150 V, 0.06 M H₃PO₄; b) 120 V, 0.42 M H₃PO₄; c) 60 V, 0.3 M H₂C₂O₄. An Al film without SiO₂ is treated in the same conditions as reference samples. The chronoamperometric evolution and the charge density passed with time are presented in Figure 3. The charge density is always approximately the same for all samples in all conditions, consistent with the fact that the thickness of anodized Al is identical within experimental uncertainty. The charges that pass through the electrode are the same, indicating that the whole Al layer has been anodized. However, in each set of conditions the anodization durations are about 20–25% shorter for the pre-patterned Al layers than for their non-patterned counterparts. This is due to the faster kinetics of the first two initial stages of the anodization

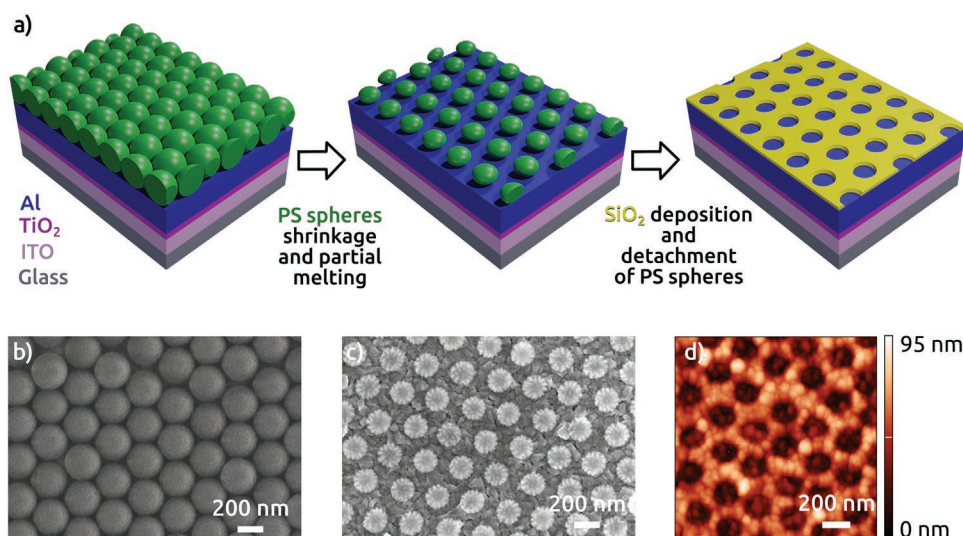


Figure 2. a) Scheme of the fabrication steps of the nanosphere lithography pattern on top of the aluminum layer on transparent substrates; b) SEM micrographs of polystyrene spheres (diameter = 280 nm) monolayer transferred onto the substrate; c) after shrinking the PS spheres down to 180 nm; d) atomic force microscopy image of SiO₂ patterned layer evaporated through the gaps of the PS spheres.

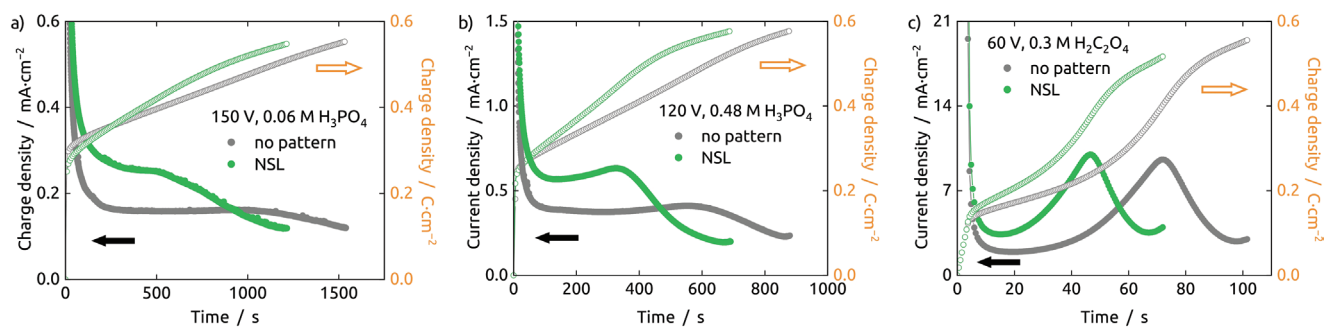


Figure 3. Chronoamperometric behavior (solid dots) and the corresponding charge density evolution (hollow dots) of the anodization of a 200 nm thick Al layer in a) 0.06 M H_3PO_4 at 150 V; b) 0.42 M H_3PO_4 at 120 V; c) 0.3 M $\text{H}_2\text{C}_2\text{O}_4$ at 60 V.

associated with the growth of a barrier alumina layer and pore nucleation^[82–84] on the patterned layers since the anodic current concentrates more easily on the Al spots exposed in the SiO_2 openings than on the bare Al layers. The anodization must be stopped when the current density reaches a minimum, after which continued anodic treatment would only result in bubble evolution and delamination of the layer (Figure S6, Supporting Information).

2.2. Evaluation of Order Degree of NSL Pre-Patterned AAO

Top-view SEM micrographs of the non-patterned nanoporous AAO samples show the typical disordered pattern obtained after first anodization (left-hand side columns on **Figure 4**). The corresponding self-correlation images (SCIs, right-hand side columns) do not reveal any pattern in either high or low magnifications. Even a clear ring around the central spot

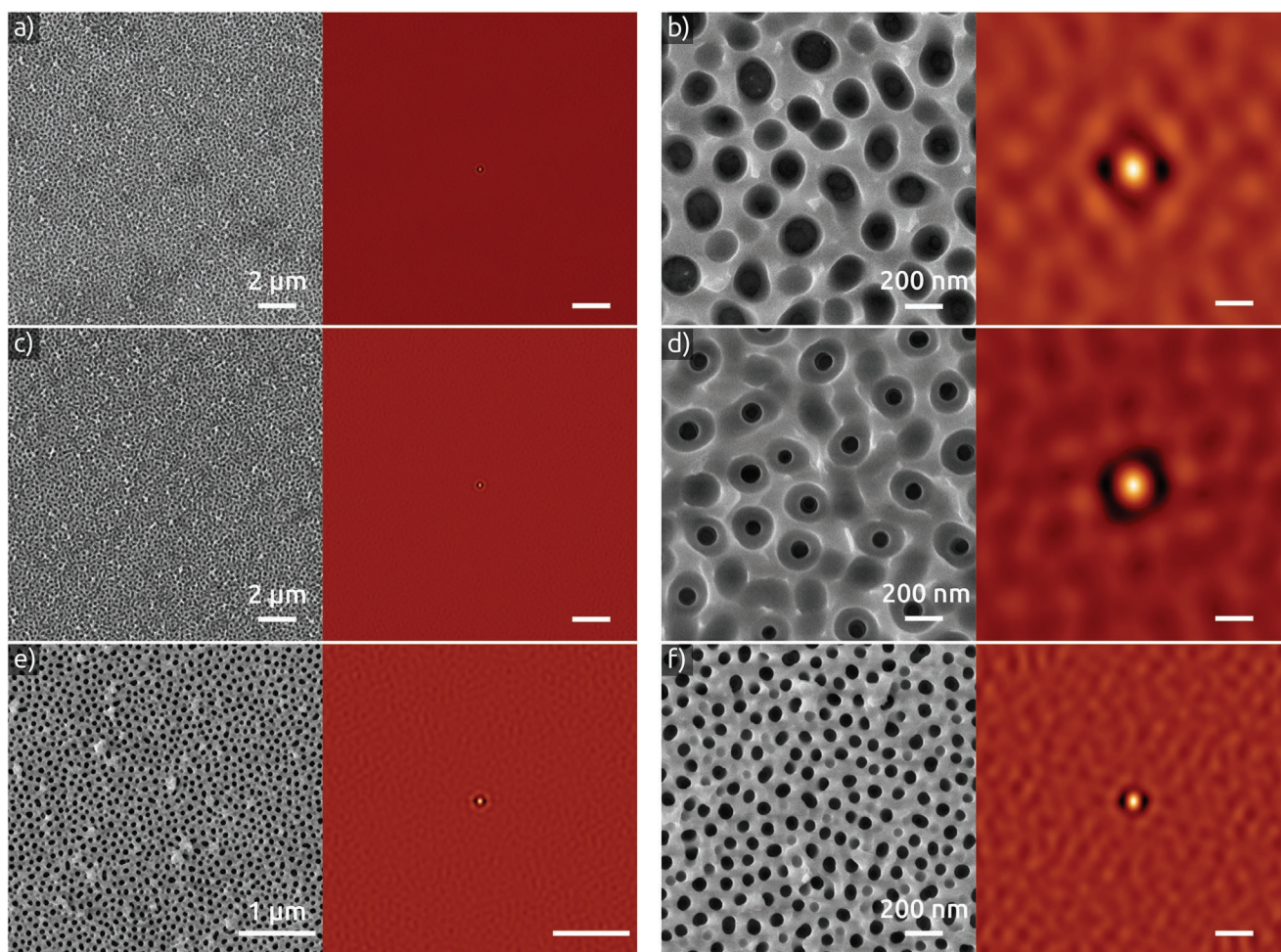


Figure 4. Top view SEM micrographs and their corresponding self-correlation images of non-patterned nanoporous AAO layers after pore widening anodized on glass / ITO / TiO_2 substrates under in a, b) 0.06 M H_3PO_4 at 150 V; c, d) 0.42 M H_3PO_4 at 120 V; e, f) 0.3 M $\text{H}_2\text{C}_2\text{O}_4$ at 60 V. The scale bars on the self-correlation images are the same as in the SEM micrographs.

Table 1. Interpore distances and estimated percentage of nanopores with open barrier layer.

Voltage – electrolyte	No pattern		NSL pre-pattern	
	Interpore distance [nm]	Open pores [%]	Interpore distance [nm]	Open pores [%]
150 V – 0.06 M H ₃ PO ₄	271 ± 7	64	279 ± 1	94
120 V – 0.42 M H ₃ PO ₄	276 ± 12	62	276 ± 2	96
60 V – 0.30 M H ₂ C ₂ O ₄	118 ± 2	80	130, 278 ± 10	99

is missing, indicating rather inhomogenous interpore distances. Radial averaging of the SCIs yields damped oscillations (Figure S7, Supporting Information) that allow one to extract the average interpore distance for the first neighbors, **Table 1**. Interestingly, the samples anodized at two distinct voltages in phosphoric acid (in two different concentrations) exhibit very similar interpore distance values (271 and 276 nm), consistent with the fact that the systems are not self-ordered. They are, however, very close to the period defined in the previous paragraph by NSL. Expectedly, anodization in oxalic acid yields a much smaller nearest-neighbor average distance.

Moreover, the distorted morphology of non-patterned nanoporous AAO films affects the barrier layer, as well. The fact that in the non-patterned case pore nucleation does not occur simultaneously at all sites causes anodization to proceed at different stages at the same time. These differences become irrelevant when long nanopores are eventually grown because the exchange of ions regulates the growth at the barrier layer. In the case of short pores in low aspect ratio as considered here, however, the short time frame of pore nucleation does lead to significant irregularities.^[79] In Figure 4a,b some pores can be observed which are still in the nucleation stage, whereas others are already in the growth phase. The various lengths of the pores, and thereby thicknesses of the oxide layer at their extremity, implies that upon subsequent wet chemical etching of this so-called “barrier oxide” only a certain fraction of them will be in direct contact to the underlying anatase TiO₂ layer (Table 1).

The samples anodized from the preliminarily patterned Al/SiO₂ system reproduce the hexagonally ordered pattern defined in SiO₂ using NSL, as enabled by the good match noted above between the naturally occurring period of the not-so-ordered system and that defined by NSL. The top-view micrographs and their corresponding SCIs in **Figure 5a,c,e** micrographs reveal a highly ordered array of nanopores with domains that extend over areas of thousands of square-micrometers (see also Figures S8 and S9, Supporting Information for low-magnification data exhibiting a perfectly ordered system over more than 85 × 150 μm). The results of the evaluation of nanopores defect density reveal a percentage of 4.2% (Figure S10, Supporting Information) and correlates perfectly with the value obtained on the analysis of the defects on the PS sphere monolayer. These perfectly arranged domains have areas one order of magnitude larger than the ones presented previously using NSL.^[50] In the higher magnification SEM micrographs, Figure 5b,d,f, one can even discern the thin SiO₂ mesh still attached to the underlying anodic alumina.

The nearest-neighbor interpore distance obtained by phosphoric acid anodization in the pre-patterned case matches that defined by NSL perfectly (Table 1), and a single pore grows

from each nucleation site. The naturally occurring distance in the case of oxalic acid anodization carried out at 60 V allows for the nucleation of three to four pores within each SiO₂ opening. This is clearly reflected in the micrograph and its corresponding SCI, although the analysis of the SCI of the sample anodized in oxalic is more complex due to the double contribution of the SiO₂ pattern and the nanopores of anodic alumina. It clearly reveals the SiO₂ pattern as being the distance between the brighter spots at 280 nm. Additionally, this SCI hints at a secondary characteristic distance on the order of 130 nm, which stands for the interpore distance within each SiO₂ opening. GISAXS data (Figure S11, Supporting Information) are also consistent with an internal structure with order at 130 nm for the AAO layer anodized at 60 V.

The ideal hexagonal geometry of the SiO₂ openings exposing the underlying Al facilitates a simultaneous initiation of pore nucleation and subsequent growth. This harmony in the formation of hexagonal arranged pores is reflected in the morphology of the pore structure as observed in cross-section, Figure S12, Supporting Information. Not only does the well-defined nucleation lead to the homogeneous formation of straight pores, a direct consequence of it is that when the barrier layer is dissolved via chemical etching, all pore extremities become open simultaneously, in contrast to the disordered nanoporous structure (the numbers presented in Table 1 refer to automated image analyses performed on at least 10 μm²). This observation of significant differences between ordered and disordered pore systems (the latter improving the fraction of open pores from ≈63% to ≈95% and from 80% to 99% in phosphoric and oxalic electrolytes) is of utmost importance for any application of such systems in the electrochemical, photoelectrochemical, or photovoltaic realms. Indeed, pores featuring remnants of the barrier layer of oxide are electrically insulated and thereby non-functional. In the ordered case, a slight “inverted shape” of the barrier layer is visible, a well-known phenomenon that takes place when anodization stops on an underlying semi-conducting substrate.^[78,85] Here the anatase TiO₂ interlayer is instrumental in protecting the TCO while the barrier layer of aluminum oxide is removed chemically in acid and preventing delamination of the porous layer from its substrate.

2.3. Proof of Function of Transparent Electrodes

A systematic characterization of the UV–vis transmittance spectra of the substrates and the electrodes is presented in **Figure 6**. Glass / ITO substrates demonstrate a transmittance of ≈90% and an absorption edge at 350 nm. When such a substrate is coated with TiO₂, the transmittance is reduced to ≈80% and the absorption edge shifts to 370 nm due to the absorption

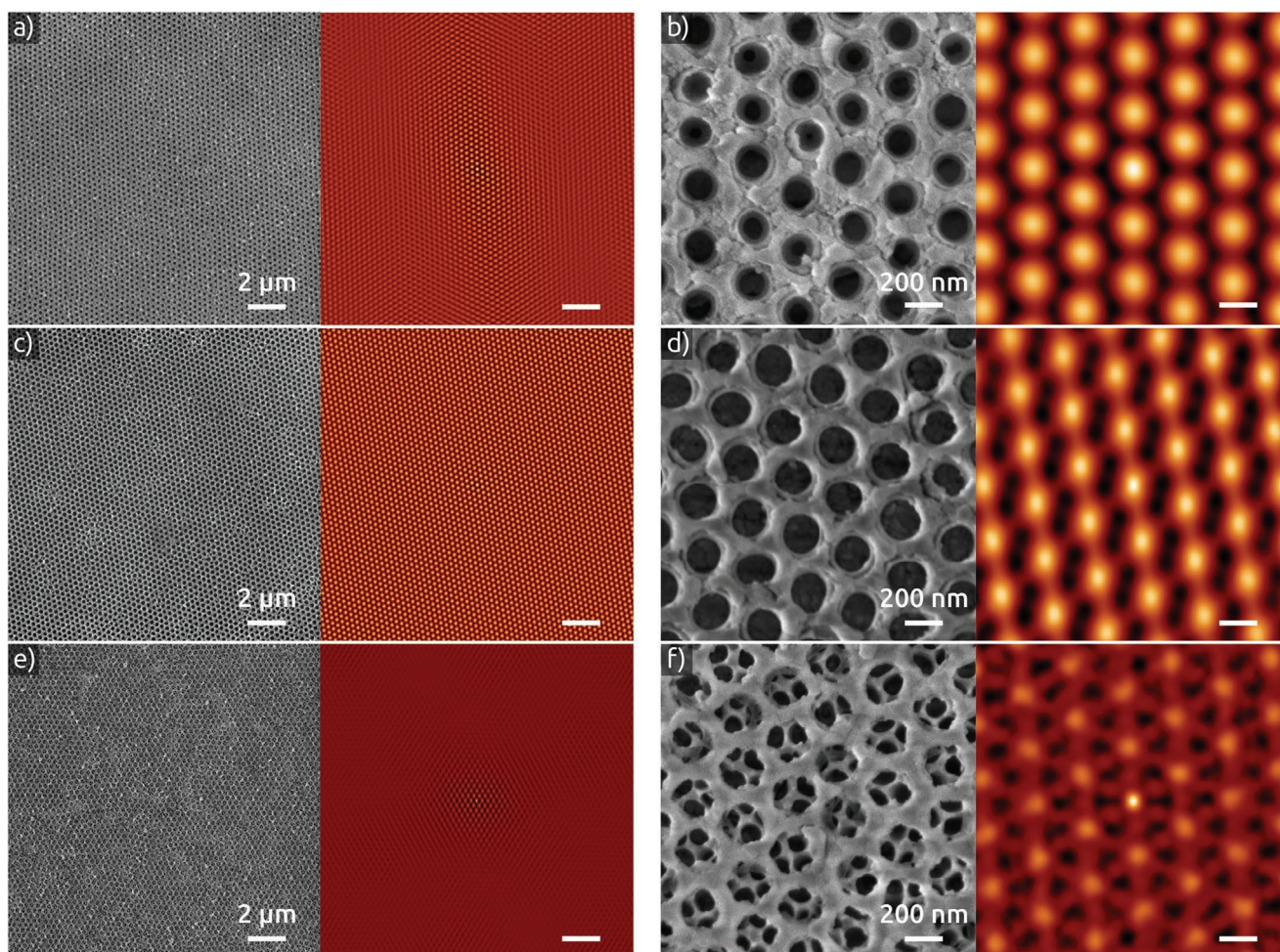


Figure 5. Top view SEM micrographs and their corresponding self-correlation images of nanoporous AAO layers grown on NSL pre-patterned glass/ITO/TiO₂/Al substrates after pore widening anodized under in a,b) 0.06 M H₃PO₄ at 150 V; c,d) 0.42 M H₃PO₄ at 120 V; e,f) 0.3 M H₂C₂O₄ at 60 V. The scale bars on the self-correlation images are the same as in the SEM micrographs.

of TiO₂. The AAO layers do not modify the transmittance spectrum significantly. The fringes caused by interference oscillate between 90% and 70%. The alumina anodized at lower voltages in oxalic acid electrolytes present slightly higher transmittance than the ones anodized at higher voltages in phosphoric acid, whereas the AAO layer anodized in phosphoric without pre-patterning exhibits the lowest transmittance. In other words, the nanostructured electrodes are optically very close to the simple, planar TCOs commercially available.

To evaluate how the nanocylindrical structure of the transparent electrodes affects their function in a solar energy conversion device, we fabricate a series of solar cells based on the templates described above and Sb₂S₃ as the light absorber, using the preparative procedures described in Section 3. An amorphous layer of TiO₂ deposited first by ALD provides a conformal coating (18 nm) of the nanoporous AAO to permit the extraction of negative charge carriers. The subsequent deposition of Sb₂S₃ is preceded by an ultrathin interfacial layer of ZnS serving to prevent dewetting of Sb₂S₃ during the crystallization process upon annealing. Samples without ultrathin ZnS interfacial layer reveals severe dewetting after crystallization (Figure S13, Supporting Information).^[86] All samples feature the stibnite phase of Sb₂S₃ as demonstrated by XRD (Figure S14,

Supporting Information). The 600 ALD cycles performed here for Sb₂S₃ are the equivalent of depositing 35 nm on a planar

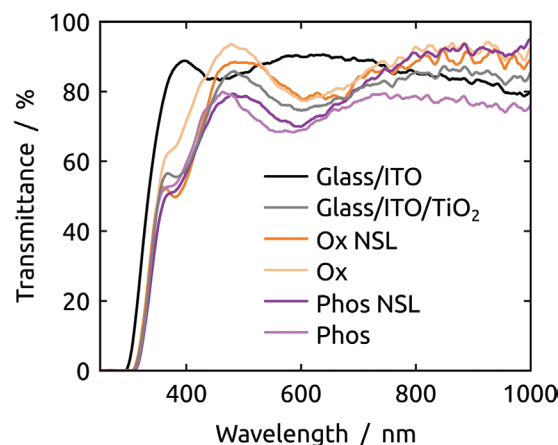


Figure 6. UV-visible transmittance spectra measured from the glass side of the substrates glass / ITO (black line), glass / ITO / TiO₂ (gray), and the AAO layers grown in oxalic acid based electrolytes with and without NSL (dark and light orange, respectively) and on phosphoric based electrolytes (dark and light purple).

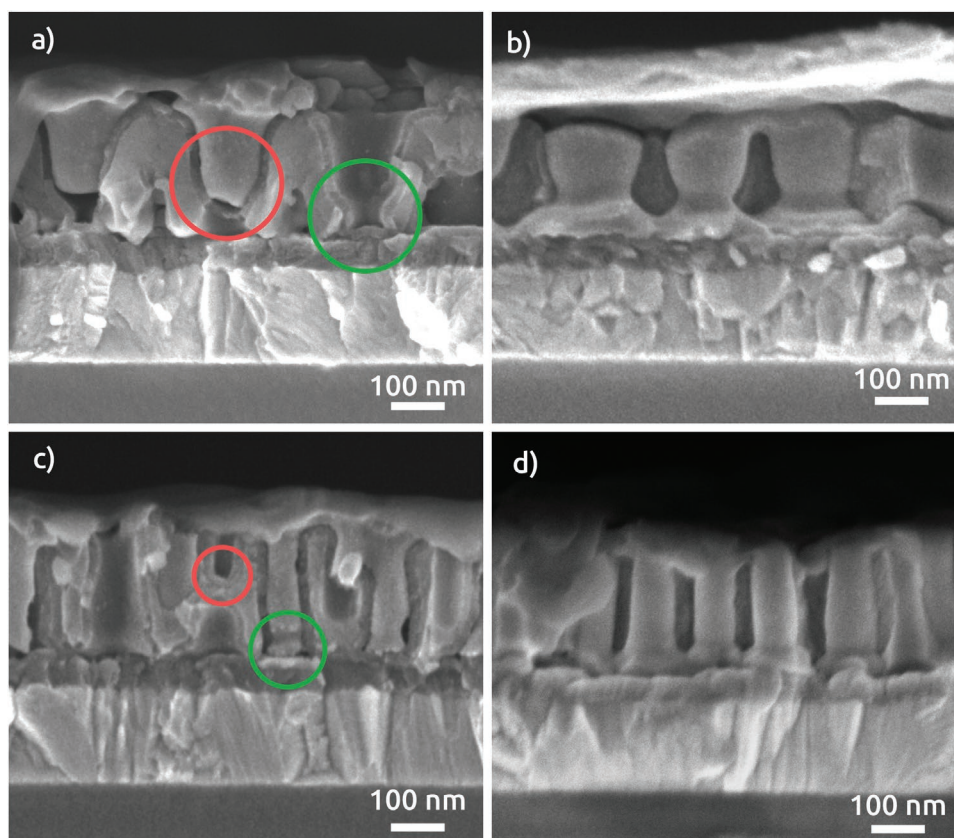


Figure 7. Cross-section electron micrographs of solar cells prepared from disordered (a,c) and ordered (b,d) pore templates anodized in a,b) phosphoric and c,d) oxalic acid. Ordered pores yield regular cylinders all of which are in contact with the TCO layer, whereas disordered ones feature pores of various geometries and correspondingly cylinders some of which are insulated from the TCO.

surface, and in the confined volume of the pores they are sufficient to fill the pores completely without forming a significant overlayer upon annealing (Figure S15, Supporting Information). Subsequently, P3HT and PEDOT:PSS are spin-coated to extract holes and a gold contact evaporated finally.

The cross-sections of the resulting photovoltaic devices (Figure 7) show the success of the preparative procedures in that the pores are filled effectively. However, the cells made from disordered substrates exhibit significant numbers of pores in which the ALD-TiO₂ layer remains without contact to the underlying sputtered TiO₂ (see for example the red highlights in Figure 7a,c), in addition to the pores in which the electrical contact is established properly (green highlights in Figure 7a,c). The ordered substrates exhibit a much more homogeneous quality of the Sb₂S₃/TiO₂ rods, all of which seem to be in good contact to the TCO.

This structural difference between ordered and disordered systems is apparent in the functional performance of the devices. The fact that all of them have similar optical properties means that any difference in the short-circuit current densities J_{SC} can be directly interpreted as a consequence of the quality of electrical contacts. Indeed, the evaluation of a statistically significant number of individual cells shows that the open-circuit voltage V_{OC} is not affected by the substrate type, indicating the the fundamental photophysics are identical. The values lie uniformly between 550 and 600 mV (Figure S16b, Supporting

Information). Fill factor and efficiencies vary more widely and the mean values present higher values on pre-patterned electrodes than on their disordered counterparts (Figure S16c,d, Supporting Information). Most importantly, a direct correlation is found, as expected, between median J_{SC} values and the percentage of open pores presented in Table 1. The direct linear dependence presented in Figure 8 provide the perfect demonstration that disordered pore arrays leave a significant fraction of pores without electrical contacts. It emphasize the importance of controlling the morphology of the pores toward photoelectrochemical or photovoltaic model applications, and thus, highlights the relevance of our NSL ordering method for short nanocylindrical electrode arrays.

3. Conclusions

In short, we have been able to self-assemble monolayers of polystyrene spheres into perfectly ordered domains of thousands of square micrometers. A transparent mask generated from them yields straight, cylindrical anodic aluminum oxide nanopore arrays that reproduce the hexagonal order. This materials system is completely transparent to visible light making it a perfect model system in which transport and interfacial phenomena can be studied for solar energy conversion technologies. Furthermore, it features nearly all pores in electrical contact to

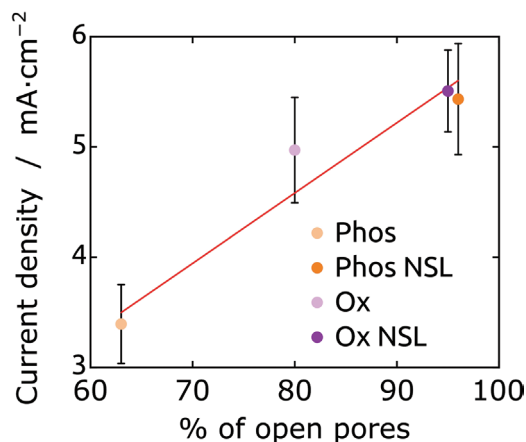


Figure 8. Correlation between the fraction of pores open at both extremities and the short-circuit current density obtained from the TCO/TiO₂/Sb₂S₃/P3HT/PEDOT:PSS/Au solar cells presented in Figure 7.

the underlying TCO, in stark contrast to comparable disordered systems. In essence, preparative procedures based on nanosphere lithography lift a significant limitation in fundamental investigation of device photophysics in the photovoltaic and photoelectrochemical realms and enables systematic studies of effect of geometric parameters in opto-electronic devices.

4. Experimental Section

Al Substrate Fabrication: ITO-coated glass substrates purchased from Techinstro with a sheet resistance of 10 Ω sq⁻¹ were first cleaned by sonication in Hellmanex (2% in Millipore water), acetone, and isopropanol for 5 min each and subjected to UV-ozone cleaning for 30 min before use. A blocking layer of 50 nm amorphous TiO₂ (TiO₂ target, 99.99%) was deposited by radio frequency sputtering (CRC 622 model, Torr International, Inc.) at a working pressure of 4.3 Pa with a power density of 2.5 W cm⁻², resulting in a deposition rate of 0.1 Å s⁻¹. Afterward the samples were annealed at 500 °C for 1 h on a hot plate in ambient conditions. Immediately before Al deposition the substrates were again cleaned by a UV-ozone treatment for 30 min. 200 nm of Al film were thermally evaporated from Al pellets (99.999%) using a Copav system from Angstrom Engineering Inc. The deposition rate was 1.3 Å s⁻¹.

Polystyrene Spheres Self-Assembly: Colloids are synthesized by surfactant-free emulsion polymerization with acrylic acid as co-monomer as described elsewhere.^[49] The colloidal solution containing PS spheres (2 wt%) was subjected to a cleaning process.^[87] The same volume of ethanol was added to the colloidal solution. This solution was centrifuged at 11,000 revolutions per minute during 10 min. After removing the liquid phase, the PS spheres were redispersed in half of the original volume in milli-Q water to double the concentration. The cleaned colloidal dispersion of 280 nm diameter polystyrene (PS) spheres (4 wt%) was diluted in ethanol (Sigma-Aldrich, 99.9%) and HCl (0.1 M, Carl Roth) with a ratio 5:4:1, resulting in a final dispersion of PS spheres of 2 wt%. Self-assembly was performed using the air-water interface as a template following an established protocol.^[50] The colloidal solution was pumped onto the air-water interface using a syringe-pump (Legato111; KD Scientific Holliston) at a speed rate of 20 μL min⁻¹ until the whole surface was filled with a close-packed monolayer of PS spheres.

Pre-Patterning of Al Substrates: The pre-assembled colloidal monolayer was transferred to the substrate (2.0 × 2.5 cm²) by immersing the sample vertically into the water subphase and pulling it up at a slightly

tilted angle. The sample was left to dry in vertical position and the highly ordered monolayer of PS spheres were attached to the surface.

The self-assembled PS spheres monolayers transferred to the substrates were etched under oxygen plasma treatment (Diener Electronic, Femto) with a flow rate of 5 sccm and applying 50% power for 9 min to shrink the diameter of the PS spheres.

SiO₂ layers were deposited via reactive evaporation of silicon monoxide (Sigma-Aldrich, powder 325 mesh) in a custom-built thermal evaporator (Torr International Inc., THE3-KW) using the following experimental parameters: 4 sccm oxygen, partial pressure of ≈ 4.0 × 10⁻⁴ Torr).

Aluminum Layer Anodization: The Al thin films were anodized at 0 °C in 0.06 and 0.42 M phosphoric acid (85.0%, VWR), and 0.3 M oxalic acid (VWR) electrolytes. The anodization voltages and the resulting currents were applied and recorded with a SourceMeter 2450 Keithley.

The anodization was stopped when the current reaches a minimum, indicating that the Al layer had been consumed and the sample had turned transparent. The resulting AAO layers were chemically etched to widen the nanopores and dissolve the barrier layer. Nanoporous AAO layers anodized in H₃PO₄ aqueous electrolytes were immersed in 10 wt% H₃PO₄ for 7 min, and those anodized in H₂C₂O₄ are etched in 5 wt% H₃PO₄ for 5 min while keeping the solutions at 45 °C. The samples were rinsed thoroughly with deionized water and afterward dried with N₂.

Solar Cell Fabrication: TiO₂ ALD was performed with an Arradiance Gemstar XT Benchtop reactor. Precursors were titanium(IV) isopropoxide and water and were kept at 70 °C and room temperature, respectively. The chamber temperature was 150 °C. The deposition rate was 0.5 Å s⁻¹. The samples were subsequently UV-ozone cleaned for 30 min and transferred to the ALD chamber for the deposition of the light absorber. Precise details of the deposition of the materials system are described in a previous work.^[81] In brief, 10 cycles of ZnS were deposited in a home-made hot-wall ALD reactor at 150 °C followed by 600 cycles of Sb₂S₃ in the same reactor without breaking the vacuum. The reactants are diethylzinc (95%, abcr), tris(dimethylamido)antimony (TDMASb, 99.99%, Sigma-Aldrich,) and hydrogen sulfide (3% in N₂, Air Liquide). The as-deposited absorber layer is annealed in a N₂-filled glovebox on a hotplate at 300 °C for 2 min. Poly-3-hexylthiophene (P3HT, regioregular, Sigma Aldrich, 15 mg mL⁻¹ in chlorobenzene) was dynamically spin-coated under ambient conditions as the hole selective layer at 6000 rpm for 1 min and dried on at hotplate at 90 °C in a N₂-filled glovebox. An additional layer of poly(3,4-ethylenedioxythiophene) polystyrene sulfonate (PEDOT:PSS, HTL solar, Ossila) was spun at 6000 rpm for 1 min with an acceleration of 6000 rpm s⁻¹ and again dried on at hotplate at 90 °C in a N₂-filled glovebox. Finally, 80 nm of Au were evaporated forming an active device area of 0.075 cm².

Characterization: GIXRD diffractograms were recorded at an incident angle of 1.3° on a Bruker D8 Advance with a Cu K_α source and a LynxEye XE T detector.

High-resolution scanning electron microscopy (SEM) images were taken with a Gemini 500, Carl-Zeiss microscope. The self-correlation images of the SEM micrographs were obtained using the open software WSxM.^[88]

The percentage of defects was calculated using a custom written MATLAB code which tracked the particles and holes in the SEM images and performed a nearest neighbor analysis. Precise details of the working principles of the software can be found in a previous work.^[89] The SEM images were converted to black and white and the particles were subsequently tracked by using the MATLAB function “imfindcircles” while the holes were tracked using the function “regionprops”. The number of neighbors was obtained by applying a Voronoi tessellation.

Atomic force microscopy (AFM) analysis was performed with NTEGRA-Prima setup in tapping mode in areas of 1.5 × 1.5 μm with 256 points/line resolution.

Grazing incidence small angle X-ray scattering measurements were performed in a customized versatile advanced X-ray scattering instrument Erlangen (VAXSTER) system equipped with a Metal Jet D2 70 kV X-ray source (λ = 1.34 Å).^[90,91] The beam was shaped to a size of 0.1 × 0.3 mm². The samples were mounted on a yzθ goniometer

allowing to adjust the grazing incidence angle of 0.3° . This angle is larger than SiO_2 critical angle ($\alpha_{\text{mc}} = 0.2^\circ$) ensuring a beam penetration of several hundreds of nanometers in the nanoporous layer and allowing for investigation of the underlying structures. The grazing incidence geometry of the incident X-ray with respect to the sample surface was used here to enhance the scattered intensity, to maximize the scattering volume, and to access the 3D structure of the electrodes studied. The scattered radiation was collected at a sample-to-detector distance (SDD) of 1.598 m. Structural information was obtained with horizontal (q_x) and vertical (q_z) cuts of the 2D intensity patterns.

The thickness of the as-grown ALD layers was determined by spectroscopic ellipsometry (SENpro, Sentech).

A solar simulator (Newport) equipped with a Xe lamp source was calibrated to AM1.5 (100 mW cm^{-2}) with a reference Si solar cell (Newport) for photovoltaic characterization. Electrical data were recorded using a single-channel Gamry Reference 600 instrument.

Supporting Information

Supporting Information is available from the Wiley Online Library or from the author.

Acknowledgements

This work was funded by the European Commission via a Marie Skłodowska-Curie Grant ('Hybriclyl', grant agreement 795716), by the European Research Council with a Consolidator Grant ('Solacylin', grant agreement 647281), by the Deutsche Forschungsgemeinschaft (DFG, German Research Foundation) in its Coordinated Research Center 'CLINT' (SFB 1452, project 431791331), by a bilateral RFBR-DFG project (RFBR 20-58-12015, DFG 429730598) and by a bilateral RFBR-DFG project (RFBR 20-58-12015, DFG 429730598). The authors acknowledge the 'Physics Educational Centre' of the Research Park of Saint Petersburg State University for technical support.

Open access funding enabled and organized by Projekt DEAL.

Conflict of Interest

The authors declare no conflict of interest.

Data Availability Statement

Data available in article supplementary material. The data that supports the findings of this study are available in the supplementary material of this article.

Keywords

anodic alumina, nanosphere lithography, self-assembly

Received: January 25, 2021

Revised: March 3, 2021

Published online: April 4, 2021

[1] Q. Wei, F. Xiong, S. Tan, L. Huang, E. H. Lan, B. Dunn, L. Mai, *Adv. Mater.* **2017**, 29, 1602300.

[2] T. J. Kempa, R. W. Day, S.-K. Kim, H.-G. Park, C. M. Lieber, *Energy Environ. Sci.* **2013**, 6, 719.

- [3] A. I. Hochbaum, P. Yang, *Chem. Rev.* **2010**, 110, 527.
- [4] L. Wen, Z. Wang, Y. Mi, R. Xu, S.-H. Yu, Y. Lei, *Small* **2015**, 11, 3408.
- [5] X. Kong, K. Zong, S. S. Lee, *Chem. Mater.* **2019**, 31, 4953.
- [6] J. T. Hu, T. W. Odom, C. M. Lieber, *Acc. Chem. Res.* **1999**, 32, 435.
- [7] S. Barth, F. Hernandez-Ramirez, J. D. Holmes, A. Romano-Rodriguez, *Prog. Mater. Sci.* **2010**, 55, 563.
- [8] I. Mínguez-Bacho, M. Courté, C. Shi, D. Fichou, *Mater. Lett.* **2015**, 159, 47.
- [9] W. Lee, S.-J. Park, *Chem. Rev.* **2014**, 114, 7487.
- [10] M. A. Einarsrud, T. Grande, *Chem. Soc. Rev.* **2014**, 43, 2187.
- [11] U. S. Mohanty, *J. Appl. Electrochem.* **2011**, 41, 257.
- [12] N. P. Dasgupta, J. Sun, C. Liu, S. Brittman, S. C. Andrews, J. Lim, H. Gao, R. Yan, P. Yang, *Adv. Mater.* **2014**, 26, 2137.
- [13] B. D. Gates, Q. Xu, M. Stewart, D. Ryan, C. G. Willson, G. M. Whitesides, *Chem. Rev.* **2005**, 105, 1171.
- [14] W.-B. Jung, S. Jang, S.-Y. Cho, H.-J. Jeon, H.-T. Jung, *Adv. Mater.* **2020**, 32, 1907101.
- [15] F. Hong, R. Blaikie, *Adv. Opt. Mater.* **2019**, 7, 1801653.
- [16] X. A. Zhang, I. T. Chen, C. H. Chang, *Nanotechnology* **2019**, 30, 352002.
- [17] X. N. Xie, H. J. Chung, C. H. Sow, A. T. S. Wee, *Mater. Sci. Eng., R* **2006**, 54, 1.
- [18] R. Garcia, R. V. Martinez, J. Martinez, *Chem. Soc. Rev.* **2006**, 35, 29.
- [19] R. C. Furneaux, W. R. Rigby, A. P. Davidson, *Nature* **1989**, 337, 147.
- [20] H. Masuda, K. Fukuda, *Science* **1995**, 268, 1466.
- [21] O. Jessensky, F. Muller, U. Gosele, *Appl. Phys. Lett.* **1998**, 72, 1173.
- [22] A. P. Li, F. Muller, A. Birner, K. Nielsch, U. Gosele, *J. Appl. Phys.* **1998**, 84, 6023.
- [23] A. P. Li, F. Muller, A. Birner, K. Nielsch, U. Gosele, *J. Vac. Sci. Technol., A* **1999**, 17, 1428.
- [24] K. Nielsch, J. Choi, K. Schwirn, R. B. Wehrspohn, U. Gosele, *Nano Lett.* **2002**, 2, 677.
- [25] S. Ono, M. Saito, H. Asoh, *Electrochim. Acta* **2005**, 51, 827.
- [26] I. Mínguez-Bacho, S. Rodríguez-López, A. Asenjo, M. Vázquez, M. Hernández-Vélez, *Appl. Phys. A: Mater. Sci. Process.* **2012**, 106, 105.
- [27] X. Qin, J. Zhang, X. Meng, C. Deng, L. Zhang, G. Ding, H. Zeng, X. Xu, *Appl. Surf. Sci.* **2015**, 328, 459.
- [28] T. Kikuchi, O. Nishinaga, S. Natsui, R. O. Suzuki, *Electrochim. Acta* **2015**, 156, 235.
- [29] S. Z. Chu, K. Wada, S. Inoue, M. Isogai, Y. Katsuta, A. Yasumori, *J. Electrochem. Soc.* **2006**, 153, B384.
- [30] W. Lee, R. Ji, U. Gosele, K. Nielsch, *Nat. Mater.* **2006**, 5, 741.
- [31] S. Z. Chu, K. Wada, S. Inoue, M. Isogai, A. Yasumori, *Adv. Mater.* **2005**, 17, 2115.
- [32] S. Y. Zhao, K. Chan, A. Yelon, T. Veres, *Adv. Mater.* **2007**, 19, 3004.
- [33] K. Schwirn, W. Lee, R. Hillebrand, M. Steinhart, K. Nielsch, U. Gosele, *ACS Nano* **2008**, 2, 302.
- [34] W. Lee, J. C. Kim, *Nanotechnology* **2010**, 21, 48.
- [35] I. Mínguez-Bacho, S. Rodríguez-López, M. Vázquez, M. Hernández-Vélez, K. Nielsch, *Nanotechnology* **2014**, 25, 145301.
- [36] D. Losic, M. Lillo, *Small* **2009**, 5, 1392.
- [37] W. Lee, R. Scholz, U. Gosele, *Nano Lett.* **2008**, 8, 2155.
- [38] C.-Y. Liu, S. Biring, *Microporous Mesoporous Mater.* **2019**, 287, 71.
- [39] J. M. M. Moreno, M. Waleczek, S. Martens, R. Zierold, D. Gorlitz, V. V. Martinez, V. M. Prida, K. Nielsch, *Adv. Funct. Mater.* **2014**, 24, 1857.
- [40] W. Lee, R. Ji, C. A. Ross, U. Gosele, K. Nielsch, *Small* **2006**, 2, 978.
- [41] H. Asoh, K. Nishio, M. Nakao, T. Tamamura, H. Masuda, *J. Electrochem. Soc.* **2001**, 148, B152.
- [42] L. Wen, R. Xu, Y. Mi, Y. Lei, *Nat. Nanotechnol.* **2017**, 12, 244.
- [43] R. Xu, L. Wen, Z. Wang, H. Zhao, G. Mu, Z. Zeng, M. Zhou, S. Bohm, H. Zhang, Y. Wu, E. Runge, Y. Lei, *Adv. Funct. Mater.* **2020**, 30, 2005170.
- [44] T. S. Kustandi, W. W. Loh, H. Gao, H. Y. Low, *ACS Nano* **2010**, 4, 2561.

- [45] N.-W. Liu, A. Datta, C.-Y. Liu, C.-Y. Peng, H.-H. Wang, Y.-L. Wang, *Adv. Mater.* **2005**, *17*, 222.
- [46] Z. J. Sun, H. K. Kim, *Appl. Phys. Lett.* **2002**, *81*, 3458.
- [47] X. Xu, Q. Yang, N. Wattanatorn, C. Zhao, N. Chiang, S. J. Jonas, P. S. Weiss, *ACS Nano* **2017**, *11*, 10384.
- [48] X. Liang, R. Dong, J. C. Ho, *Adv. Mater. Technol.* **2019**, *4*, 1800541.
- [49] N. Vogel, L. de Viguier, U. Jonas, C. K. Weiss, K. Landfester, *Adv. Funct. Mater.* **2011**, *21*, 3064.
- [50] I. Mínguez-Bacho, F. Scheler, P. Büttner, K. Bley, N. Vogel, J. Bachmann, *Nanoscale* **2018**, *10*, 8385.
- [51] D. Ji, T. Li, H. Fuchs, *Nano Today* **2020**, *31*, 100843.
- [52] S. Fournier-Bidoz, V. Kitaev, D. Routkevitch, I. Manners, G. Ozin, *Adv. Mater.* **2004**, *16*, 2193.
- [53] A. L. Lipson, D. J. Comstock, M. C. Hersam, *Small* **2009**, *5*, 2807.
- [54] M. Krupinski, M. Perzanowski, A. Maximenko, Y. Zabala, M. Marszalek, *Nanotechnology* **2017**, *28*, 194003.
- [55] Y. Hu, X. Wang, M. Zhang, S. Wang, S. Li, G. Chen, *Nano Lett.* **2021**, *21*, 250.
- [56] C. Mijangos, R. Hernández, J. Martín, *Prog. Polym. Sci.* **2016**, *54-55*, 148.
- [57] J. Martín, M. Martín-González, J. Francisco Fernández, O. Caballero-Calero, *Nat. Commun.* **2014**, *5*, 5130.
- [58] J. Martín, M. Dyson, O. G. Reid, R. Li, A. Nogales, D.-M. Smilgies, C. Silva, G. Rumbles, A. Amassian, N. Stingelin, *Adv. Electron. Mater.* **2018**, *4*, 1700308.
- [59] J. Ko, Y. Kim, J. S. Kang, R. Berger, H. Yoon, K. Char, *Adv. Mater.* **2020**, *32*, 1908087.
- [60] O. de Melo, E. M. Larramendi, I. Mínguez-Bacho, S. Larramendi, J. L. Baldonedo, J. M. M. Duart, M. Hernandez-Velez, *J. Cryst. Growth* **2008**, *311*, 26.
- [61] E. Berganza, C. Bran, M. Jaafar, M. Vázquez, A. Asenjo, *Sci. Rep.* **2016**, *6*, 29702.
- [62] S. Iglesias-Freire, C. Bran, E. Berganza, I. Mínguez-Bacho, C. Magén, M. Vázquez, A. Asenjo, *Nanotechnology* **2015**, *26*, 395702.
- [63] I. Mínguez-Bacho, S. Rodríguez-López, A. Climent, D. Fichou, M. Vázquez, M. Hernández-Vélez, *J. Phys. Chem. C* **2015**, *119*, 27392.
- [64] I. Mínguez-Bacho, S. Rodríguez-López, A. Climent-Font, D. Fichou, M. Vázquez, M. Hernández-Vélez, *Microporous Mesoporous Mater.* **2016**, *225*, 192.
- [65] A. Christoulaki, C. Moretti, A. Chennevière, E. Dubois, N. Jouault, *Microporous Mesoporous Mater.* **2020**, *303*, 110201.
- [66] A. Christoulaki, A. Chennevière, I. Grillo, L. Porcar, E. Dubois, N. Jouault, *J. Appl. Crystallogr.* **2019**, *52*, 745.
- [67] K. S. Choudhari, S. D. Kulkarni, C. Santhosh, S. D. George, *Microporous Mesoporous Mater.* **2018**, *271*, 138.
- [68] V. Yakovtseva, D. Shimanovich, V. Sokol, A. Subko, V. Bondarenko, *MRS Adv.* **2018**, *3*, 569.
- [69] S. Y. Lim, C. S. Law, L. Jiang, L. K. Acosta, A. Bachhuka, L. F. Marsal, A. D. Abell, A. Santos, *ACS Appl. Nano Mater.* **2020**, *3*, 12115.
- [70] H.-C. Kwon, A. Kim, H. Lee, D. Lee, S. Jeong, J. Moon, *Adv. Energy Mater.* **2016**, *6*, 1601055.
- [71] H. Wu, J. Yang, S. Cao, L. Huang, L. Chen, *Macromol. Chem. Phys.* **2014**, *215*, 584.
- [72] Y. Wu, L. Assaud, C. Kryschi, B. Capon, C. Detavernier, L. Santinacci, J. Bachmann, *J. Mater. Chem. A* **2015**, *3*, 5971.
- [73] N. Haberkorn, J. S. Gutmann, P. Theato, *ACS Nano* **2009**, *3*, 1415.
- [74] D. Chen, W. Zhao, T. P. Russell, *ACS Nano* **2012**, *6*, 1479.
- [75] Q. Hao, H. Huang, X. Fan, X. Hou, Y. Yin, W. Li, L. Si, H. Nan, H. Wang, Y. Mei, T. Qiu, P. K. Chu, *Nanotechnology* **2017**, *28*, 105301.
- [76] A. Al-Haddad, Z. Zhan, C. Wang, S. Tarish, R. Vellacheria, Y. Lei, *ACS Nano* **2015**, *9*, 8584.
- [77] S. Z. Chu, K. Wada, S. Inoue, S. Todoroki, *J. Electrochem. Soc.* **2002**, *149*, B321.
- [78] T. R. B. Foong, A. Sellinger, X. Hu, *ACS Nano* **2008**, *2*, 2250.
- [79] P. Liu, V. P. Singh, S. Rajaputra, *Nanotechnology* **2010**, *21*, 115303.
- [80] Y. Lin, Q. Lin, X. Liu, Y. Gao, J. He, W. Wang, Z. Fan, *Nanoscale Res. Lett.* **2015**, *10*, 495.
- [81] P. Büttner, D. Döhler, S. Korenko, S. Möhrlein, S. Bochmann, N. Vogel, I. Mínguez-Bacho, J. Bachmann, *RSC Adv.* **2020**, *10*, 28225.
- [82] V. P. Parkhutik, V. I. Shershulsky, *J. Phys. D: Appl. Phys.* **1992**, *25*, 1258.
- [83] K. Shimizu, K. Kobayashi, G. E. Thompson, G. C. Wood, *Philos. Mag. A* **1992**, *66*, 643.
- [84] G. Thompson, *Thin Solid Films* **1997**, *297*, 192.
- [85] D. Crouse, Y.-H. Lo, A. E. Miller, M. Crouse, *Appl. Phys. Lett.* **2000**, *76*, 49.
- [86] P. Büttner, F. Scheler, C. Pointer, D. Döhler, M. K. S. Barr, A. Koroleva, D. Pankin, R. Hatada, S. Flege, A. Manshina, E. R. Young, I. Mínguez-Bacho, J. Bachmann, *ACS Appl. Energy Mater.* **2019**, *2*, 8747.
- [87] M. Rey, T. Yu, R. Guenther, K. Bley, N. Vogel, *Langmuir* **2019**, *35*, 95.
- [88] I. Horcas, R. Fernández, J. M. Gómez-Rodríguez, J. Colchero, J. Gómez-Herrero, A. M. Baro, *Rev. Sci. Instrum.* **2007**, *78*, 013705.
- [89] J. Harrer, M. Rey, S. Ciarella, H. Löwen, L. M. C. Janssen, N. Vogel, *Langmuir* **2019**, *35*, 10512.
- [90] M. Berlinghof, C. Bär, D. Haas, F. Bertram, S. Langner, A. Osvet, A. Chumakov, J. Will, T. Schindler, T. Zech, C. J. Brabec, T. Unruh, *J. Synchrotron Radiat.* **2018**, *25*, 1664.
- [91] C. Zhang, T. Heumueller, W. Gruber, O. Almora, X. Du, L. Ying, J. Chen, T. Unruh, Y. Cao, N. Li, C. J. Brabec, *ACS Appl. Mater. Interfaces* **2019**, *11*, 18555.